



## PAPER

[View Article Online](#)  
[View Journal](#) | [View Issue](#)Cite this: *Dalton Trans.*, 2024, **53**,  
15937Relaxometric properties and biocompatibility of a  
novel nanostructured fluorinated gadolinium  
metal–organic framework†Letizia Trovarelli,<sup>‡a</sup> Alessandra Mirarchi,<sup>‡b</sup> Cataldo Arcuri,<sup>\*,b</sup> Stefano Bruscoli,<sup>b</sup>  
Oxana Bereshchenko,<sup>b</sup> Marta Febo,<sup>b</sup> Fabio Carniato <sup>\*c</sup> and  
Ferdinando Costantino <sup>\*a</sup>

A novel Gd-MOF based on tetrafluoro-terephthalic acid has been synthesized and its structure has been solved using X-ray single crystal diffraction data. The compound, with the formula  $[\text{Gd}_2(\text{F}_4\text{BDC})_3 \cdot \text{H}_2\text{O}] \cdot \text{DMF}$ , is isostructural with other Ln-MOFs based on the same ligand and has been recently reported. Its crystals were also reduced to nanometer size by employing acetic acid or cetyltrimethylammonium bromide (CTAB) as a modulator. The relaxometric properties of the nanoparticles were evaluated in solution by measuring  $^1\text{H}$   $T_1$  and  $T_2$  as a function of the applied magnetic field and temperature. The biocompatibility of Gd-MOFs was evaluated on murine microglial BV-2 and human glioblastoma U251 cell lines. In both cell lines, Gd-MOFs do not modify the cell cycle profile or the activation levels of ERK1/2 and Akt, which are protein-serine/threonine kinases that participate in many signal transduction pathways. These pathways are fundamental in the regulation of a large variety of processes such as cell migration, cell cycle progression, differentiation, cell survival, metabolism, transcription, tumour progression and others. These data indicate that Gd-MOF nanoparticles exhibit high biocompatibility, making them potentially valuable for diagnostic and biomedical applications.

Received 24th July 2024,  
Accepted 2nd September 2024

DOI: 10.1039/d4dt02134g

[rsc.li/dalton](http://rsc.li/dalton)

## Introduction

Magnetic resonance imaging (MRI) is nowadays considered one of the most promising techniques in the field of diagnostic imaging as it is non-invasive, versatile, non-ionizing and can be used for many anatomic and biochemical investigations for the detection of tissue pathologies.<sup>1</sup> The methodology is based on the measure of the relaxation times of different isotopes having a nonzero magnetic moment upon the influence of an external magnetic field. For practical and routine purposes,  $^1\text{H}$  nuclei belonging to water molecules are the chemical species mostly used in MR as they display high sensitivity in terms of relaxation under a magnetic field. Moreover, the

distribution of water molecules reflects the structural composition of tissue, as changes in the water properties of the tissue also closely reflect pathological processes.<sup>2</sup> Gd-chelates such as Gd-DOTA, Gd-DTPA and Gd-HPDO3A (DOTA = 2,2',2'',2'''-(1,4,7,10-tetraazacyclododecane-1,4,7,10-tetrayl)tetraacetic acid; DTPA = 2,2',2'',2'''-[(carboxymethyl)-azanediy]bis(ethane-2,1-diynitrilo)}tetraacetic acid; HP-DO3A = 2,2',2''-[10-(2-hydroxypropyl)-1,4,7,10-tetraazacyclododecane-1,4,7-triyl] triacetic acid) are benchmark compounds for *in vivo* MRI imaging because of their ability to influence the relaxation rate of the water and then improve the image contrast.<sup>3</sup> In this way, the signal intensity on  $T_1$ -weighted images is increased, which can reduce the acquisition time, improve diagnostic confidence and finally, reduce artefacts and overall costs. The  $\text{Gd}^{3+}$  ion shows excellent relaxation because of the presence of a high effective magnetic moment, a spherical distribution of electrons in f orbitals and long electron relaxation times.<sup>3</sup>

Despite its use in diagnostics, free gadolinium can be toxic *in vitro* and *in vivo* for several reasons. It can interfere with calcium channels, altering the transmission of cellular signals. It can also precipitate causing the deposition of gadolinium salts and altering normal cellular and tissue functions. In humans, contrast agents with gadolinium are known to be toxic to the kidneys and the liver, and for this reason, in

<sup>a</sup>Department of Chemistry, Biology and Biotechnologies, University of Perugia, Via Elce di Sotto n 8, 06123 Perugia, Italy. E-mail: [ferdinando.costantino@unipg.it](mailto:ferdinando.costantino@unipg.it)<sup>b</sup>Department of Medicine and Surgery, University of Perugia, Piazza Lucio Severi 1, 06132 Perugia, Italy<sup>c</sup>Department of Science and Technological Innovation, University of Eastern Piedmont “A. Avogadro”, Viale Teresa Michel 11, 15121 Alessandria, Italy†Electronic supplementary information (ESI) available: Additional SEM and TEM figures. MRI profiles for MOF nanocrystals. CCDC 2362133 for Gd-F<sub>4</sub>BDC. For ESI and crystallographic data in CIF or other electronic format see DOI: <https://doi.org/10.1039/d4dt02134g>

‡These authors contributed equally.

people with renal failure, they must be administered under strict medical supervision.<sup>4–6</sup> A possible accumulation of gadolinium in the central nervous system has also recently been highlighted.<sup>7</sup> However, the use of chelating substances limits these risks by facilitating their elimination at the renal level and limiting their reactivity.

Although it is not common for gadolinium-based contrast agents to cross the blood–brain barrier (BBB) under normal conditions, there are specific circumstances in which they can enter the central nervous system. In the presence of pathologies that compromise the BBB integrity, such as inflammation, brain tumors, trauma, and infections, gadolinium-based contrast agents can penetrate the CNS enhancing MRI images of the lesions. Edema associated with stroke, haemorrhage, or other brain injury can also cause disruption of the BBB, allowing gadolinium to enter the CNS.<sup>8–10</sup>

Among the contrast agents that contain gadolinium, gadoversetamide represents a classic example. Approved at the end of the 90s by the FDA as a contrast medium to be used for images of the brain and spinal cord, in subsequent years it was less used due to its renal toxicity and was replaced by contrast agents with a macrocyclic structure with an improved safety profile. For these reasons, further studies aimed at improving the safety profiles of gadolinium contrast agents are necessary. In a recent study,<sup>11</sup> gold nanoparticles conjugated with gadolinium and epidermal growth factor were synthesized. These nanoparticles exhibit good biocompatibility in a human breast adenocarcinoma cell line, demonstrating how similar studies are crucial to hypothesize new compounds that can be used for clinical diagnosis with lower risks for patients.

Among the materials used as contrast agents, metal–organic frameworks (MOFs), containing different paramagnetic ions, are rapidly emerging, and the number of compounds used as MRI agents both *in vivo* and *in vitro* in the last ten years has sensibly increased.<sup>12</sup> However, MOFs as MRI probes are currently confined to research purposes and not intended for clinical applications. MOFs are porous crystalline materials constituted of the ordered connections of metals or metallic clusters with polytopic linkers generally based on carboxylates or N-containing heterocyclic compounds.<sup>13</sup> Other than the good performances of these materials in terms of contrast ability in MRI, low toxicity and stability under biological conditions are two other mandatory issues to be considered for the application of MOFs in diagnostic applications.

MOFs based on paramagnetic ions such as Gd(III), Mn(II) and Fe(III) have already been employed for MRI application.<sup>12</sup> Gd-based MOFs have been mainly constructed by using carboxylic ligands such as simple terephthalic or trimesic acid or more complex acids such as *N*-(4-carboxybenzyl)-(3,5-dicarboxyl)-pyridinium bromide or 5-boronobenzene-1,3-dicarboxylate.<sup>3,12</sup> Crystal size reduction to the nanometer scale has been found to be very important in order to increase the stability and dispersibility in biological liquid media and also in influencing the relaxivity parameters.<sup>12,14,15</sup> In the present paper we report on a Gd-MOF based on 1,4-tetrafluoro-terephthalic acid as a ligand<sup>16</sup> and on its relaxivity properties.

The MOF was obtained as a single crystal in a DMF/water/EtOH mixture and its structure was characterized by single crystal X-ray diffraction. The use of acetic acid or a surfactant namely CTAB as a crystallinity modulator allows one to obtain MOF nanoparticles with a size below 60 nm.<sup>17–19</sup>

To evaluate the biocompatibility of these nanoparticles, Gd-MOF NPs were tested in two different cell types of nervous origin, microglia and astrocytic tumours. Microglial cells are the primary immune cells residing within the central nervous system's tissue. They carry out various and intricate tasks, including preserving the neural environment, immune surveillance, and repairing damage. Additionally, they have recently been recognized for their roles in phagocytosis during normal brain development and the selective removal of synapses, which sculpts neural circuits in the postnatal period. Furthermore, they contribute to neuronal proliferation and differentiation and neurogenesis.<sup>20</sup> U251 is a human glioblastoma (GBM) cell line. GBM is the most malignant (IV grade of WHO classification) brain tumour being characterized by a short clinical course with a median survival of only 14.6 months. This tumour includes cells with extremely immature morphology and a significant decrease in GFAP expression.<sup>21</sup> We therefore evaluated whether the internalization of these NPs could influence the activity of two fundamental signalling pathways mediated by serine/threonine kinases ERK1/2 and Akt.

The ERK1/2 signalling pathway is triggered by a diverse array of receptors linked to growth and differentiation, such as receptor tyrosine kinases (RTKs), ion channels, and integrins. Activated ERK1/2 can then modulate targets within the cytoplasm and move to the nucleus, where it phosphorylates various transcription factors that control gene expression. ERK1/2 plays a key role in controlling microglial activation, leading to the release of pro-inflammatory cytokines. They also impact microglial cell proliferation and survival. GBM has also been associated with the components of the MAPK pathways and mutations of ERK1/2.<sup>22</sup>

As ERK1/2, Akt regulates multiple biological processes including proliferation, glycogen metabolism, and cell survival. Various growth factors, cytokines, hormones activate it.

Akt is involved in the regulation of microglial activation. Its activation can be triggered by several signals, including those from cytokine and growth factor receptors. In microglia, Akt activation can contribute to their survival during stress conditions or injury and modulate the inflammatory response by influencing the expression of genes involved in the production of cytokines and inflammatory mediators. It may be involved in both the promotion and inhibition of the inflammatory response. Dysfunctional activation of Akt may contribute to the progression of neurodegenerative diseases and, in brain tumours, *i.e.* GBM, various mutations have been identified that enhance the intrinsic kinase activity of PI3K. The high incidence of aberrant Akt signalling in human diseases has led to the intensive development of small molecule inhibitors targeting PI3K and Akt.<sup>22</sup> In the present paper we report the synthesis, structure and size reduction to the nanometer range of a novel Gd MOF, along with its MRI relaxation properties



and *in vitro* cell viability on murine microglial BV-2 and human glioblastoma U251 cell lines.

## Experimental section

### Materials and methods

The metal salt, organic linker and all the solvents used were directly available from suppliers and used as received. Powder X-ray diffraction (PXRD) patterns were collected with a Bruker diffractometer D8 ADVANCE with a Cu-K $\alpha$ 1,2 anode ( $\lambda = 1.5406 \text{ \AA}$ ). Mercury software was used for data visualization. Single-crystal diffraction (SC-XRD) data were collected with a Bruker D8 VENTURE. The X-ray source was a Microfocus molybdenum K $\alpha$ 1 anode ( $\lambda = 0.71073 \text{ \AA}$ ). FT-IR ATR spectra were obtained using a PerkinElmer spectrometer, Vertex 70 model. A Varian-700 ES was used for ICP-OES analysis. Thermogravimetric analysis (TGA) was carried out on a NETZSCH STA 449 Jupiter. Transmission electron microscopy (TEM) images were collected with an EM 400 T model (HT range 20–120 kV). Relaxometric data were collected by measuring the magnetic-field dependence of the longitudinal relaxation rate ( $R_1$ ) in aqueous solution by using a variable field relaxometer equipped with an HTS-110 3T Metrology Cryogen-free Superconducting Magnet (Mede, Italy), operating in the overall range of proton Larmor frequencies of 20–120 MHz (0.47–3.00 T). The measurements were performed using the standard inversion recovery sequence (20 experiments, 2 scans) with a typical 90° pulse width of 3.5  $\mu\text{s}$  and the reproducibility of the data was within  $\pm 0.5\%$ . The temperature was controlled with a Stelar VTC-91 heater airflow. Additional points in the 0.01–10 MHz frequency range were collected on a Fast-Field Cycling (FFC) Stelar SmarTracer Relaxometer. Transversal relaxation rate values ( $R_2$ ) are measured in the 0.5–3.0 T range at 298 K. All the experiments are repeated three times with the reproducibility of the data within  $\pm 0.5\%$ .

**Synthesis of Gd-F<sub>4</sub>BDC (1).** The Gd-F<sub>4</sub>BDC MOF was prepared by facile solvothermal synthesis, mixing Gd(NO<sub>3</sub>)<sub>3</sub>·6H<sub>2</sub>O (0.5 mmol) and F<sub>4</sub>BDC (0.5 mmol) in 9 mL of dimethylformamide (DMF), 9 mL of ethanol and 7 mL of water in a Teflon reactor. The mixture was heated at 80 °C for 24 hours. Then, the product was washed under vacuum, adding a few milliliters of ethanol, water, and acetone. The solid was dried overnight at 40 °C. ICP-OES analysis: Gd(III) calculated 37 wt%, experimental 35 wt%. Yield: 23%.

**Synthesis of Gd-F<sub>4</sub>BDC (2).** The synthesis of the Gd-F<sub>4</sub>BDC MOF was optimized, reducing the amount of solvents required. Gd(NO<sub>3</sub>)<sub>3</sub>·6H<sub>2</sub>O (0.5 mmol) and F<sub>4</sub>BDC (0.5 mmol) were mixed in 2 mL of dimethylformamide (DMF), 2 mL of ethanol and 1 mL of water in a Teflon reactor. The mixture was heated at 80 °C for 24 hours. Then, the product was washed under vacuum, adding a few milliliters of ethanol, water, and acetone. The solid was dried overnight at 40 °C. ICP-OES analysis: Gd(III) calculated 37 wt%, experimental 32 wt%. Yield: 22%.

**Synthesis of Gd-F<sub>4</sub>BDC (3).** The Gd-F<sub>4</sub>BDC MOF can also be synthesized by avoiding DMF and using  $\gamma$ -valerolactone (GVL).

In particular, Gd(NO<sub>3</sub>)<sub>3</sub>·6H<sub>2</sub>O (0.5 mmol) and F<sub>4</sub>BDC (0.5 mmol) were added to 5 mL of GVL in a Teflon reactor. The mixture was heated at 120 °C for 24 hours. Then, the product was washed under vacuum, adding a few milliliters of GVL, ethanol, water, and acetone. The solid was dried overnight at 40 °C. ICP-OES analysis: Gd(III) calculated 37 wt%, experimental 33 wt%. Yield: 31%.

**Synthesis of Gd-F<sub>4</sub>BDC NPs.** Gd-F<sub>4</sub>BDC MOF nanoparticles were synthesized by adding to the previous mixture (synthesis of 2) two types of modulators: acetic acid (1 mmol) (synthesis of 4) and the surfactant CTAB (0.005 mmol) (synthesis of 5).

**Cell culture conditions.** The U251 cell line was purchased from CLS Cell Line Services (product number 300385) (Eppelheim, Deutschland). The BV-2 cell line, that is not commercially available, was obtained in our laboratories by Bocchini *et al.* (1993).<sup>23</sup> U251 and BV-2 cell lines were grown in DMEM with high glucose (EuroClone S.p.A., Milano, Italy) supplemented with 10% FBS (EuroClone S.p.A., Milano, Italy), 100 IU mL<sup>-1</sup> penicillin G, and 100  $\mu\text{g mL}^{-1}$  streptomycin (EuroClone S.p.A., Milano, Italy) under an H<sub>2</sub>O-saturated 5% CO<sub>2</sub> atmosphere at 37 °C.

**Internalization of Gd-F<sub>4</sub>BDC by U251 glioblastoma and BV-2 microglial cell lines.** Two hundred thousand cells were seeded into 35 mm Petri dish plates (Thermo Fisher Scientific, Waltham, MD, USA) in complete medium. After 24 h, the medium was renewed and 4, 8, and 12  $\mu\text{g mL}^{-1}$  Gd-F<sub>4</sub>BDC were added. After 24 h and 48 h, the culture medium was discharged, the cells were washed five times with PBS, detached with trypsin/EDTA (0.1%), collected and centrifuged (400g, 7 min). The cells were resuspended in 0.4 mL of PBS and the tubes were kept at 4 °C for at least 30 min before flow cytometric analysis. The Gd-F<sub>4</sub>BDC@Acr fluorescence of individual cells was detected with a Coulter Epics XL-MCL flow cytometer (Beckman Coulter, Brea, CA, USA) and data were analyzed using FlowJo software (TreeStar, Ashland, OR, USA).

**Measurement of the cell cycle and apoptosis.** The control and 4, 8, and 12  $\mu\text{g mL}^{-1}$  Gd-F<sub>4</sub>BDC treated cells were collected and centrifuged (400g, 7 min) in order to recover the cells in suspension. The cells were washed two times with PBS and processed for cell cycle analysis by propidium iodide staining and flow cytometry. Briefly, the cells were resuspended in 0.4 mL of hypotonic fluorochrome solution (50  $\mu\text{g mL}^{-1}$  propidium iodide in 0.1% sodium citrate plus 0.1% Triton X-100) in 12  $\times$  75 mm polypropylene tubes (BD Biosciences Italy, Milano, Italy). The tubes were kept at 4 °C for at least 30 min before flow cytometric analysis. The propidium iodide fluorescence of individual nuclei was measured using a Coulter Epics XL-MCL flow cytometer (Beckman Coulter). The percentages of cells in G0/G1, S, and G2/M phases and sub-G1 apoptotic cells were calculated using FlowJo software (TreeStar).

**Western blotting.** The cells were cultivated for 24 h in the presence of 4, 8, and 12  $\mu\text{g mL}^{-1}$  Gd-F<sub>4</sub>BDC, washed twice with phosphate-buffered saline (PBS) and solubilized with 20% SDS, 1 M Tris-HCl pH 7.4, 1 M dithiothreitol, 200 mM PMSF, 10 mg mL<sup>-1</sup> aprotinin (Gold Biotechnology, St Louis, MO, USA), 1 mg mL<sup>-1</sup> pepstatin (EuroClone S.p.A., Milano, Italy)



and 5 mg mL<sup>-1</sup> leupeptin (SERVA Electrophoresis GmbH, Heidelberg, Germany). Equal amounts of cell lysates were separated through 10% SDS PAGE. The following antibodies were used: polyclonal anti-phosphorylated (serine 473) Akt (1 : 1000), polyclonal anti-total Akt (1 : 1000), polyclonal anti-phosphorylated (Thr202/Tyr204) Erk1/2 (1 : 1000), and polyclonal anti-total Erk1/2 (1 : 5000) (all from Cell Signaling Technology, Leiden, The Netherlands). The immune reaction was developed using the SuperSignal West Pico Luminol/Enhancer Solution (Thermo Fisher Scientific, Waltham, MD, USA). Filters were subjected to densitometric analysis of the pertinent immune bands and their relative standard references using Image Studio Digit software (LI-COR, Lincoln, NE, USA).

## Results and discussion

### Synthesis and characterization

Three different synthetic strategies were employed for the preparation of Gd-F<sub>4</sub>BDC. Synthesis (1) employed a DMF/EtOH/H<sub>2</sub>O mixture, giving single crystals useful for structural determination. Synthesis (2) was also performed to reduce the amount of solvent needed and it was successful, although no single crystals were found. Synthesis (3) was performed in order to avoid the toxic DMF solvent by replacing it with GVL, a sustainable and harmless solvent obtained by biomass valorization.<sup>24</sup> Also in this case, the compound is pure and the diffraction patterns are in agreement with the calculated ones. The XPRD patterns of the samples obtained from the three syntheses are shown in Fig. 1. Finally, CTAB or acetic acid was used as the modulator in order to reduce the size of Gd-F<sub>4</sub>BDC and to obtain it as nanoparticles with a size in the 50–80 nm

range to be employed in relaxometric and cytotoxicity tests.<sup>17–19</sup> Gd-F<sub>4</sub>BDC obtained from the synthesis of **1** and used for crystal structure determination has the formula [Gd<sub>2</sub>(F<sub>4</sub>BDC)<sub>3</sub>·H<sub>2</sub>O]·DMF (see Table S1† for crystallographic information). It crystallizes in the monoclinic *P21/a* space group with *a* = 7.7894(2), *b* = 21.8151(6), *c* = 10.1789(3) Å, and  $\beta$  = 98.80(1)° and it has a three-dimensional structure composed of edge-sharing GdO<sub>9</sub> polyhedral chains running along the *c*-axis coordinated in the *a*–*c* plane by an *exo*-bidentate F<sub>4</sub>BDC linker, thus designing a hybrid inorganic–organic layer. The layers are pillared along the *b*-axis by another F<sub>4</sub>BDC linker, thus designing quasi-square channels of 5.5 × 6.8 Å filled by one DMF molecule. The coordination of Gd(III) ions is antiprismatic with eight oxygen atoms belonging to four monodentate and two chelating F<sub>4</sub>BDC ligands. One coordinated water molecule that makes a H-bond with the oxygen atom of the guest DMF molecule (Ow...O–C = 2.59(1) Å) completes the coordination sphere of Gd(III) ions. The structure of Gd-F<sub>4</sub>BDC is shown in Fig. 2. Gd–O bonds lie in the 2.3–2.5 Å range and the Gd–Ow distance is 2.36(1) Å. A family of Ln-F<sub>4</sub>BDC MOFs was reported by Han and co-authors in 2017.<sup>25</sup> The authors reported 16 compounds, two of which having [Ln(F<sub>4</sub>BDC)1.5(H<sub>2</sub>O)]·2H<sub>2</sub>O, Ln = Nd and Pr, crystallize in the same monoclinic system of Gd-F<sub>4</sub>BDC reported in our manuscript with similar cell parameters. In contrast, the Gd(III) compound reported in that paper has the formula [Gd(TFBDC)1.5(H<sub>2</sub>O)<sub>2</sub>]·H<sub>2</sub>O, it crystallizes in the C-centered *C2/m* space group and has a 2D layered structure with cell parameters *a* = 13.88, *b* = 11.22, *c* = 11.59 Å, and  $\beta$  = 124.9°. <sup>26</sup> An Erbium-based MOF

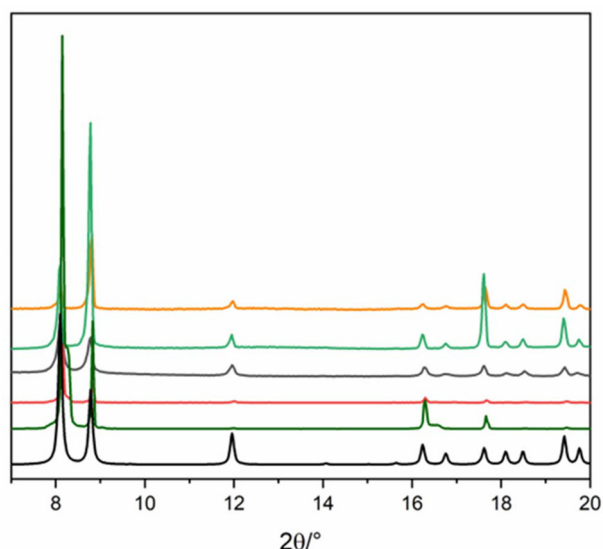


**Fig. 1** PXRD patterns of the Gd-F<sub>4</sub>BDC MOF obtained through the synthetic procedure reported: synthesis no. 1 (olive green), synthesis no. 2 (red line), synthesis no. 3 (grey line), synthesis no. 4 (orange), and synthesis no. 5 (light green). The calculated PXRD pattern is also reported (black line).

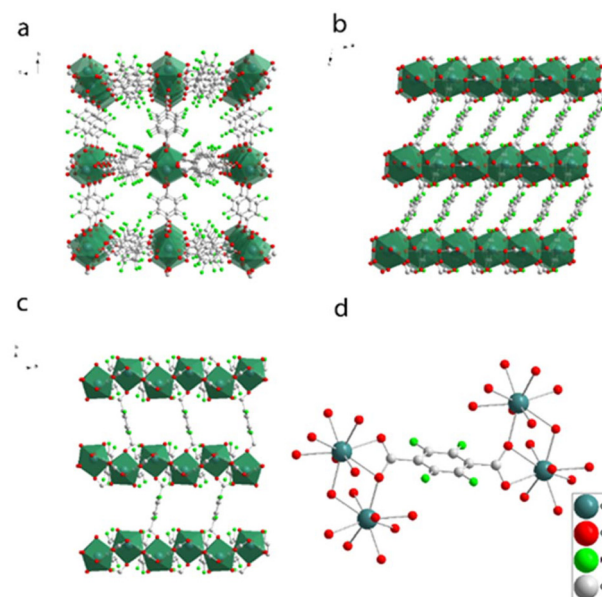


**Fig. 2** Structural framework viewed along the (a) *a*-axis, (b) *b*-axis and (c) *c*-axis respectively. (a) clearly shows the quasi-square channels. (d) shows the Gd(III) coordination sphere. Four GdO<sub>9</sub> units are connected by one 2,3,5,6-tetrafluoroterephthalic acid molecule. Colour scheme: Gd in blue, O in red, F in green and C in grey (hydrogen atoms are omitted for clarity).





almost isostructural to Gd-F<sub>4</sub>BDC and with the formula Er<sub>2</sub>(BDC-F<sub>4</sub>)<sub>3</sub>(DMF)(H<sub>2</sub>O)·DMF was also reported in 2006 by Chen and co-authors, although its coordination number (8 instead of 9) and solvent content are different with respect to our compound.<sup>27</sup> The polyhedral representation of Gd-F<sub>4</sub>BDC together with Gd(III) coordination details is shown in Fig. 2.

Fig. 3 shows the results of the modulated syntheses of Gd-F<sub>4</sub>BDC using acetic acid as the modulator. Acetic acid afforded nanoparticles with a quite large size distribution ranging from 200 to 50 nm, as depicted in Fig. 3b and c (SEM and TEM images). The synthesis with CTAB as the modulator afforded spherical shaped nanoparticles with a sharper size distribution in the 50–80 nm size range. SEM and TEM images related to nanoparticles obtained with CTAB are reported in the ESI (S2 and S3†).

The study explored the relaxometric characteristics of the Gd-F<sub>4</sub>BDC MOF nanocrystals obtained with acetic acid as the modulator by examining the proton longitudinal relaxivity ( $r_1$ ) as a function of the applied magnetic field strength (<sup>1</sup>H nuclear magnetic relaxation dispersion (NMRD) profile). The relaxivity ( $r_1$ ) is defined as the longitudinal relaxation rate of water protons, normalized to 1 mM concentration of the paramagnetic probe.<sup>28</sup> Under clinical magnetic fields of 1.5 and 3.0 T and at a temperature of 298 K, the  $r_1$  values were determined to fall within the range of 12–13 mM<sup>−1</sup> s<sup>−1</sup> (Table 1). These values are approximately three times greater than those of the commercially available low molecular weight Gd(III) probes.<sup>2</sup> The  $r_2/r_1$  values at 0.7, 1.5, and 3.0 T (Table 1) closely approximate 1, suggesting that this MOF can be considered as a positive MRI contrast agent.<sup>29–31</sup>

These findings are thoroughly examined by assessing the  $r_1$  values of the MOF aqueous suspension ([Gd<sup>3+</sup>] = 4.77 mM) in relation to the applied magnetic field, ranging from 0.01 to 120 MHz. The increase in the longitudinal relaxation rate of water protons is influenced by three primary mechanisms: the short-range interaction between the paramagnetic metal ion and the coordinated water molecule(s) (inner sphere contribution,  $r_1^{\text{IS}}$ ), the interaction involving hydrogen-bonded water molecules with the polar groups of the ligand (second sphere contribution,  $r_1^{\text{SS}}$ ), and a long-range interaction between the

**Table 1**  $r_1$  and  $r_2/r_1$  values of the nanosized Gd-F<sub>4</sub>BDC MOF at 298 K

Magnetic fields	0.7 T	1.5 T	3.0 T
$r_1$ (mM <sup>−1</sup> s <sup>−1</sup> )	11.7	12.7	12.3
$r_2/r_1$	1.0	1.1	1.0

metal ion and bulk water molecules (outer sphere contribution,  $r_1^{\text{OS}}$ ).<sup>28</sup> The active involvement of IS and SS contributions significantly influences the  $r_1$  values. The <sup>1</sup>H NMRD profiles of the nanosized Gd-F<sub>4</sub>BDC MOF at 283, 298 and 310 K are reported in Fig. 4. At 298 K, the profile consists of a low-magnetic-field plateau (0.01–1 MHz), followed by a dispersion centered at 4 MHz and a second plateau in the 20–120 MHz range. The  $r_1$  values under high magnetic fields (>0.5 T), low with respect to what is observed for other nanosystems based on Gd(III) ions,<sup>32</sup> are indicative of an average of the active Gd(III) ions on the surface, in dipolar interaction with water and the ions embedded in the nanoparticle core, not accessible to the solvent molecules and “silent” from the relaxometric point of view. Given the complexity of the system, the examination of <sup>1</sup>H NMRD profiles could only provide a

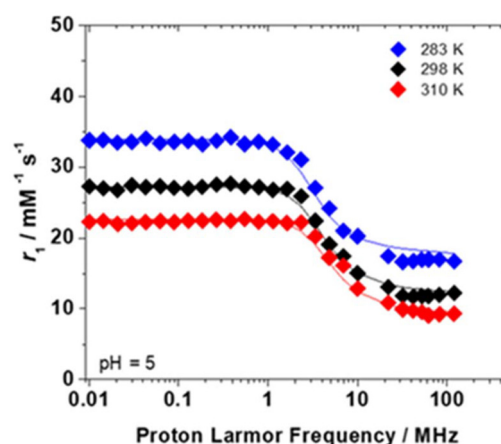


**Fig. 4** <sup>1</sup>H  $T_1$  NMRD profiles of the Gd-F<sub>4</sub>BDC MOF ([Gd<sup>3+</sup>] = 4.77 mM) at 283, 298, and 310 K.

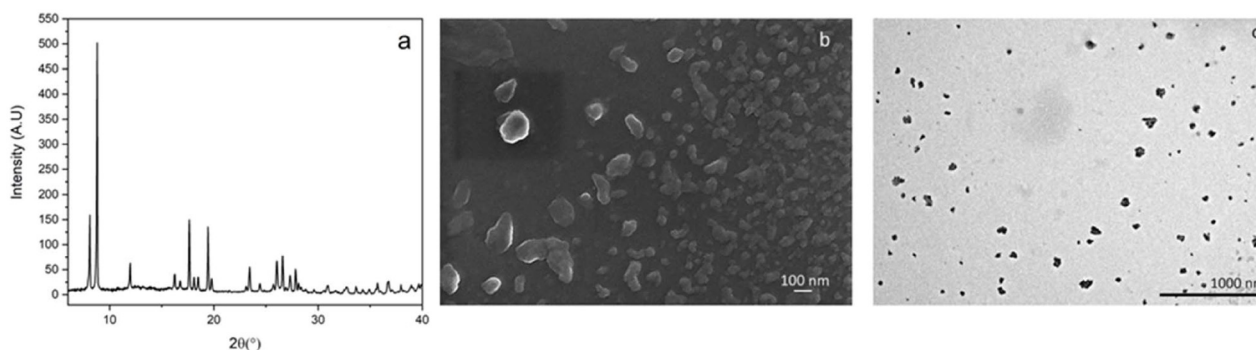


**Fig. 3** PXRD patterns of the Gd-F<sub>4</sub>BDC MOF NPs are shown in (a) (acetic acid was used as a modulator) whereas (b) and (c) show selected SEM and TEM images. Other images are reported in Fig. S4 and S5 (ESI†).



qualitative understanding of the relaxation mechanisms taking place in the solution. The  $^1\text{H}$  NMRD profile was analyzed by applying the Solomon–Bloembergen–Morgan (SBM) and Freed equations.<sup>33–36</sup>

The best results were achieved by excluding the inner-sphere contribution and fixing certain parameters to standard values.<sup>28</sup>

This approach was already applied to layered carboxyalkylaminophosphonate nanocrystals with Gd(III) ions located in the framework and coordinated to one inner sphere water in the crystal state.<sup>37</sup>

Given the significant complexity of these solids, it is challenging to find a single model that accurately fits the  $^1\text{H}$  NMRD profiles; however, a similar approach was applied to other paramagnetic MOFs documented in the literature.<sup>38</sup> The low  $r_1$  values over the entire frequency range indicate that probably only the outer and second sphere mechanisms are operative. Specifically, the distance of the closest approach of outer-sphere water ( $a$ ) was set at 4.0 Å, while the distance from the metal ion to the second sphere water molecules ( $r^{\text{SS}}$ ) was established at 3.5 Å. The diffusion coefficient at 298 K ( $D$ ) was fixed at  $2.24 \times 10^{-9} \text{ m}^2 \text{ s}^{-1}$ . Lastly, the activation energy for the modulation of zero-field splitting ( $E_v$ ) was fixed at 1 kJ mol $^{-1}$ . A reasonable fitting of the curves was achieved by considering an average of six second-sphere water molecules ( $q^{\text{SS}}$ ) in fast rotation with a  $\tau_R^{\text{SS}}$  of 99 ps, interacting with the carboxylate groups near the Gd(III) ions, coupled with an activation energy of 17 kJ mol $^{-1}$  ( $E_R^{\text{SS}}$ ), exchanging rapidly due to the open-pore structure. The parameter values governing the relaxation of the electron spin, including the mean square transient ZFS energy ( $\Delta^2$ ) and its correlation time ( $\tau_v$ ), are detailed in Table 2. The average lifetime ( $\tau_M^{\text{SS}}$ ) of second-sphere water molecules is relatively short (*ca.* 40 ns), so it does not affect relaxivity at any frequency. This is further corroborated by the observation that the relaxivity decreases with an increase in temperature along the investigated magnetic fields.<sup>28</sup>

The same relaxometric profile was also observed for the Gd-F<sub>4</sub>BDC NPs dispersed in water (6.81 mM referred to as Gd) as depicted in Fig. S6†

To assess the stability of MOF dispersion, the leaching of Gd(III) was evaluated after dispersing the MOF in phosphate buffer at pH 7 for 48 hours. Specifically, 20 mg of Gd-F<sub>4</sub>BDC was dispersed in 20 mL of phosphate buffer and stirred for 48 hours. The solid was then recovered by centrifugation of the solution and ICP-OES analysis was performed on the supernatant. 4 mL of the supernatant was filtered through cellulose

vinegar filters (filter diameter 0.2  $\mu\text{m}$ ) to remove any MOF not well separated from the solution. Finally, 3 wt% HNO<sub>3</sub> was added, and the volume was made up to 5 mL. The analytical data suggest the absence of the degradation phenomenon of the MOF in phosphate buffer, as the percentage of metal in solution is less than 0.1% (see Table S2†).

Regarding the biocompatibility of Gd-F<sub>4</sub>BDC, after a 24 hour treatment period, the uptake of the MOF stained with acridine orange was evaluated using cytofluorimetry, comparing fluorescence intensity levels. BV2 cells treated with the MOF (Fig. 5B) exhibited 100% fluorescence positivity, contrast-

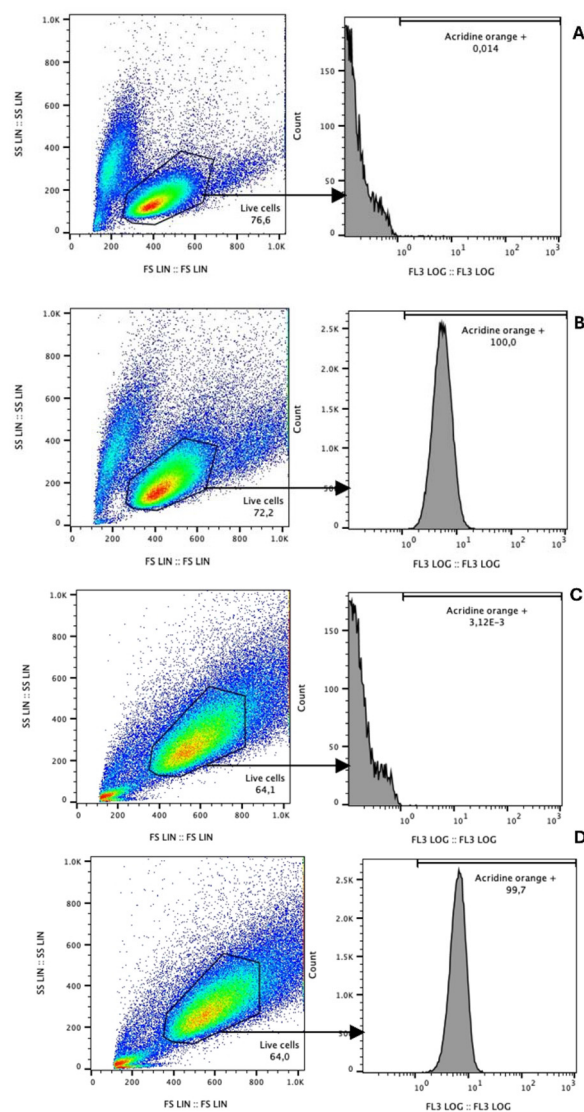


**Fig. 5** Assessment of Gd-F<sub>4</sub>BDC nanoparticle penetration into BV2 and U251 cell lines through cytofluorimetric analysis. (A and B) Representative images of acridine orange, fluorescent cells in (A) not treated with BV2 cells and (B) nanoparticles treated with BV2 cells. (C and D) Representative images of acridine orange fluorescent cells in (C) not treated with U251 cells and (D) nanoparticles treated with U251 cells. Numbers within quadrants represent the frequency of the gated populations.

**Table 2** Parameters extrapolated from the analysis of  $^1\text{H}$  NMRD data

Parameters	Gd-F <sub>4</sub> BDC MOF
$^{60}r_1$ (298 K) (mM $^{-1}$ s $^{-1}$ )	12.7
$\Delta^2/10^{18}$ s $^{-2}$	7.6
$\tau_v$ /ps	60
$\tau_R^{\text{SS}}$ /ps	99
$E_R^{\text{SS}}$ /kJ mol $^{-1}$	17
$q^{\text{SS}}$	6



ing with untreated cells (Fig. 5A), which displayed no fluorescence in the emission spectrum of acridine orange. Similarly, U251 cells demonstrated 99.7% of fluorescent cells (Fig. 5D) after 24 hours, while untreated cells (Fig. 5C) showed no positivity for acridine orange fluorescence. These results suggest the internalization of nanoparticles within the lines of interest.

Moreover, after a 24 hour treatment period, cell proliferation and apoptotic levels were evaluated using cytofluorimetry. The examination of the cell cycle in the BV2 cell line revealed no statistically significant changes in the G0/G1, S, and G2/M phases when comparing untreated cells with those treated with various concentrations of Gd-F<sub>4</sub>BDC (Fig. 6A). Similarly, there were no observed alterations in the rate of apoptosis among the analyzed cell groups (Fig. 6B). In the case of the U251 cell line, treatment with Gd-F<sub>4</sub>BDC at concentrations of 4, 8, and 12  $\mu\text{g mL}^{-1}$  showed no notable impact on the distribution of cells across different cell cycle phases (Fig. 6C), nor did it seem to influence apoptosis levels (Fig. 6D). This suggests that MOF treatment can be considered safe for cells, as it neither disrupts proliferation nor induces toxicity.

Graphs represent the mean  $\pm$  SEM. To verify the possible activation of ERK and Akt, BV2 and U251 cells were treated with Gd-F<sub>4</sub>BDC at concentrations of 4, 8, and 12  $\mu\text{g mL}^{-1}$  for 24 hours. The levels of phosphorylated ERK1/2 and Akt have

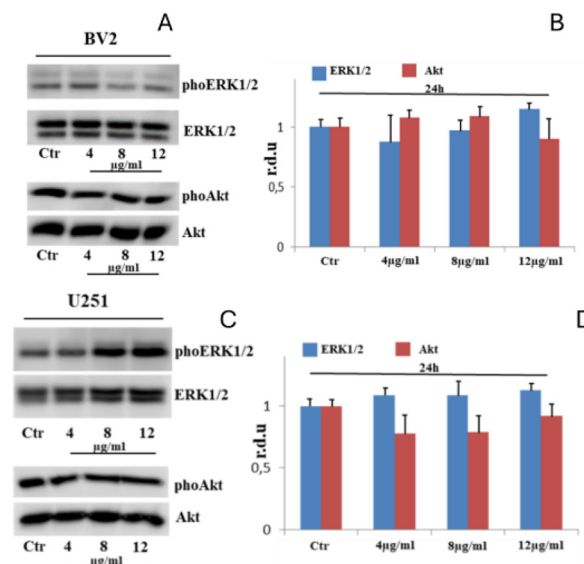


**Fig. 7** Gd-F<sub>4</sub>BDC nanoparticles do not affect Akt and ERK1/2 phosphorylation in BV2 microglia and U251 glioblastoma cells. (A) Western blots and (B) densitometric quantification of ERK1/2 and Akt levels in BV2 cells. (C) Western blots and (D) densitometric quantification of ERK1/2 and Akt levels in U251 glioblastoma cells. The cells were treated with 4, 8, and 12  $\mu\text{g mL}^{-1}$  of Gd-F<sub>4</sub>BDC for 24 h. Blots are representative of at least three experiments. The differences are not statistically significant.

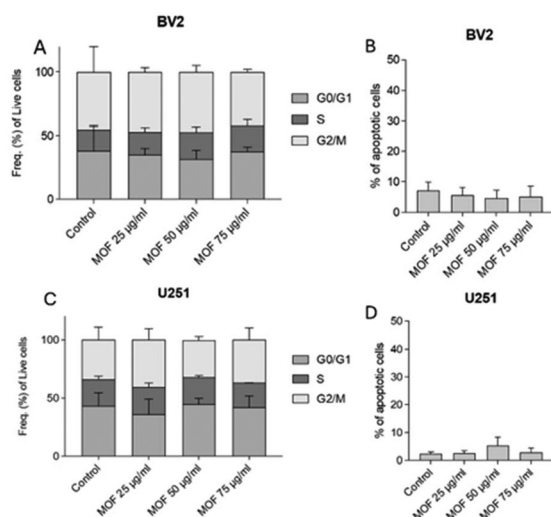


**Fig. 6** Assessment of cell cycle phases and apoptotic levels in BV2 and U251 cell lines through cytofluorimetric analysis. (A) Graphs show the frequency (%) of live cells in the G0–G1, S, and G2/M phases of the cell cycle of BV2 cells. Cells were untreated or treated with Gd-F<sub>4</sub>BDC at concentrations of 4, 8, and 12  $\mu\text{g mL}^{-1}$ . (B) Graphical representation of the frequency of apoptotic cells in BV2 untreated cells or treated with Gd-F<sub>4</sub>BDC. (C) Graphs show the frequency (%) of live cells in the G0–G1, S, and G2/M phases of the cell cycle of U251 cells. Cells were untreated or treated with Gd-F<sub>4</sub>BDC at concentrations of 4, 8, and 12  $\mu\text{g mL}^{-1}$ . (D) Graphical representation of the frequency of apoptotic cells in U251 untreated cells or treated with the same concentration of Gd-F<sub>4</sub>BDC.

been evaluated by western blotting (Fig. 7). In BV2 cells, Gd-F<sub>4</sub>BDC did not alter the phosphorylated levels of these serine/threonine kinases (Fig. 7A and B). Similarly, the levels of phosphorylated ERK and Akt were not affected in GBM cells (Fig. 7C and D). We conclude that Gd-F<sub>4</sub>BDCs have a completely inert behavior, easily penetrate inside and do not alter the metabolic properties of the cells.

## Conclusion

A novel three-dimensional Gd-MOF has been synthesized and its crystal structure was solved *ab initio* by single crystal X-ray diffraction data. Nanoparticles, ranging in size from 50 to 80 nm, were also obtained by using organic modulators in the synthesis process. The nanoparticles maintain the same crystal structure as the pristine MOF and their relaxometric properties were investigated by measuring longitudinal and transverse relaxation rates as a function of the applied magnetic field. Despite the intrinsic complexity of the system due to the varying accessibility of the paramagnetic centers, it was still possible to make a general assessment of the molecular and dynamic parameters responsible for the relaxometric behavior of the studied MOF. Furthermore, the sample exhibited improved longitudinal relaxivity values under clinical magnetic fields compared to commercially available MRI contrast agents.

The Gd-MOF shows excellent biocompatibility on microglia and glioblastoma cell lines, but further studies will be needed





in order to speculate on the Gd-MOF as a valuable carrier for MRI contrast imaging, drug and/or gadolinium delivery in the central nervous system.

## Abbreviations

CCR2 CC chemokine receptor 2  
CCL2 CC chemokine ligand 2  
CCR5 CC chemokine receptor 5  
TLC Thin layer chromatography.

## Author contributions

L. T., A. M., and M. F.: investigation and formal analysis. S. B. and O. B.: validation and data curation. F. C., C. A. and F. C.: conceptualization, supervision and writing/editing the original paper.

## Data availability

CCDC deposition number 2362133 contains the crystallographic data for Gd-F<sub>4</sub>BDC.

All other data supporting this article have been included as part of the ESI.†

## Conflicts of interest

There are no conflicts to declare.

## Acknowledgements

F. C. and L. T. acknowledge the Italian MUR through the Project PRIN 2020 doMino (ref. 2020P9KBKZ). This work has been funded by the European Union – NextGenerationEU under the Italian Ministry of University and the Research (MUR) National Innovation Ecosystem grant ECS00000041 – VITALITY. We acknowledge Università degli Studi di Perugia and MUR for support within the project VITALITY.

## References

- 1 T. Yousaf, G. Dervenoulas and M. Politis, in *International Review of Neurobiology*, Elsevier, 2018, vol. 141, pp. 31–76.
- 2 J. Wahsner, E. M. Gale, A. Rodríguez-Rodríguez and P. Caravan, *Chem. Rev.*, 2019, **119**, 957–1057.
- 3 L. Qin, Z.-Y. Sun, K. Cheng, S.-W. Liu, J.-X. Pang, L.-M. Xia, W.-H. Chen, Z. Cheng and J.-X. Chen, *ACS Appl. Mater. Interfaces*, 2017, **9**, 41378–41386.
- 4 C. Thakral, J. Alhariri and J. L. Abraham, *Contrast Media Mol.*, 2007, **2**, 199–205.
- 5 M. Rogosnitzky and S. Branch, *BioMetals*, 2016, **29**, 365–376.
- 6 N. Schieda, J. I. Blachman, A. F. Costa, R. Glikstein, C. Hurrell, M. James, P. Jabejdar Maralani, W. Shabana, A. Tang, A. Tsampalieros, C. Van Der Pol and S. Hiremath, *Can. Assoc. Radiol. J.*, 2018, **69**, 136–150.
- 7 B. J. Guo, Z. L. Yang and L. J. Zhang, *Front. Mol. Neurosci.*, 2018, **11**, 335.
- 8 T. Kanda, T. Fukusato, M. Matsuda, K. Toyoda, H. Oba, J. Kotoku, T. Haruyama, K. Kitajima and S. Furui, *Radiology*, 2015, **276**, 228–232.
- 9 N. Murata, K. Murata, L. F. Gonzalez-Cuyar and K. R. Maravilla, *Magn. Reson. Imaging*, 2016, **34**, 1359–1365.
- 10 M. Rasschaert, R. O. Weller, J. A. Schroeder, C. Brochhausen and J. Idée, *Magn. Reson. Imaging*, 2020, **52**, 1293–1305.
- 11 S. M. Queiroz, T. S. Veriato, L. Raniero and M. L. Castilho, *Radiol. Phys. Technol.*, 2024, **17**, 153–164.
- 12 H. Bunzen and D. Jiráček, *ACS Appl. Mater. Interfaces*, 2022, **14**, 50445–50462.
- 13 M. Ding, X. Cai and H.-L. Jiang, *Chem. Sci.*, 2019, **10**, 10209–10230.
- 14 A. Bieniek, A. P. Terzyk, M. Wiśniewski, K. Roszek, P. Kowalczyk, L. Sarkisov, S. Keskin and K. Kaneko, *Prog. Mater. Sci.*, 2021, **117**, 100743.
- 15 H. Zhang, Y. Shang, Y.-H. Li, S.-K. Sun and X.-B. Yin, *ACS Appl. Mater. Interfaces*, 2019, **11**, 1886–1895.
- 16 D. Morelli Venturi and F. Costantino, *RSC Adv.*, 2023, **13**, 29215–29230.
- 17 W. Morris, S. Wang, D. Cho, E. Auyeung, P. Li, O. K. Farha and C. A. Mirkin, *ACS Appl. Mater. Interfaces*, 2017, **9**, 33413–33418.
- 18 N. Liu, L. Shi and X. Meng, *J. Chem. Sci.*, 2019, **131**, 50.
- 19 S.-H. Wu and D.-H. Chen, *J. Colloid Interface Sci.*, 2004, **273**, 165–169.
- 20 C. Arcuri, C. Mecca, I. Giambanco and R. Donato, *Int. J. Dev. Neurosci.*, 2019, **77**, 26–38.
- 21 C. Arcuri, V. Bocchini, P. Guerrieri, C. Fages and M. Tardy, *J. Neurosci. Res.*, 1995, **40**, 622–631.
- 22 C. Arcuri, *Front. Biosci.*, 2017, **22**, 268–309.
- 23 V. Bocchini, R. Mazzolla, R. Barluzzi, E. Blasi, P. Sick and H. Kettenmann, *J. Neurosci. Res.*, 1992, **31**, 616–621.
- 24 D. Morelli Venturi, F. Campana, F. Marmottini, F. Costantino and L. Vaccaro, *ACS Sustainable Chem. Eng.*, 2020, **8**, 17154–17164.
- 25 J. Han, S. Zhang, Q. Wei, G. Xie and S. Chen, *Z. Anorg. Allg. Chem.*, 2017, **643**, 850–857.
- 26 Y. Han, P. Yan, J. Sun, G. An, X. Yao, Y. Li and G. Li, *Dalton Trans.*, 2017, **46**, 4642–4653.
- 27 B. Chen, Y. Yang, F. Zapata, G. Qian, Y. Luo, J. Zhang and E. B. Lobkovsky, *Inorg. Chem.*, 2006, **45**, 8882–8886.
- 28 L. Helm, J. R. Morrow, C. J. Bond, F. Carniato, M. Botta, M. Braun, Z. Baranyai, R. Pujales-Paradela, M. Regueiro-Figueroa, D. Esteban-Gómez, C. Platas-Iglesias and T. J. Scholl, in *New Developments in NMR*, ed. V. C. Pierre and M. J. Allen, Royal Society of Chemistry, Cambridge, 2017, pp. 121–242.





- 29 P. Caravan, J. J. Ellison, T. J. McMurphy and R. B. Lauffer, *Chem. Rev.*, 1999, **99**, 2293–2352.
- 30 S. Aime, M. Botta and E. Terreno, in *Advances in Inorganic Chemistry*, Elsevier, 2005, vol. 57, pp. 173–237.
- 31 S. Aime, S. G. Crich, E. Gianolio, G. B. Giovenzana, L. Tei and E. Terreno, *Coord. Chem. Rev.*, 2006, **250**, 1562–1579.
- 32 M. Botta and L. Tei, *Eur. J. Inorg. Chem.*, 2012, **2012**, 1945–1960.
- 33 I. Solomon, *Phys. Rev.*, 1955, **99**, 559–565.
- 34 N. Bloembergen, *J. Chem. Phys.*, 1957, **27**, 572–573.
- 35 N. Bloembergen and L. O. Morgan, *J. Chem. Phys.*, 1961, **34**, 842–850.
- 36 J. H. Freed, *J. Chem. Phys.*, 1978, **68**, 4034–4037.
- 37 A. Scafuri, R. Vivani, F. Carniato, L. Tei, M. Botta, M. Taddei and F. Costantino, *Dalton Trans.*, 2015, **44**, 19072–19075.
- 38 S.-Y. Zhang, Z.-Y. Wang, J. Gao, K. Wang, E. Gianolio, S. Aime, W. Shi, Z. Zhou, P. Cheng and M. J. Zaworotko, *Chem*, 2019, **5**, 1609–1618.

